Physica Scripta

INCLUSIVE PUBLISHING TRUSTED SCIENCE

PURPOSE-LED PUBLISHING™

PAPER • **OPEN ACCESS**

Test results of the DTT poloidal field conductor samples in SULTAN: DC and AC characterization

To cite this article: G De Marzi *et al* 2025 *Phys. Scr.* **100** 045605

View the article online for updates and enhancements.

You may also like

- DTT toroidal field conductor samples test in Sultan: DC and AC characterization
C Fiamozzi Zignani, G De Marzi, G Scarantino et al.
- Present Status of the KSTAR Superconducting Magnet System Development
Kim Keeman, H K Park, K R Park et al.
- Test results on systems developed for the SST-1 tokamak
D. Bora and SST-1 Team

This content was downloaded from IP address 81.57.8.77 on 19/10/2026 at 14:46

Physica Scripta

PAPER

Test results of the DTT poloidal field conductor samples in SULTAN: DC and AC characterization

G De Marzi[1], C Fiamozzi Zignani[1], H Bajas[2], R Bonifetto[3], A Di Zenobio[1], L Muzzi[1], M Ortino[2], G M Polli[1,4], G Ramogida[1,4], G Scarantino[3], K Sedlak[2], S Turtù[1] and A Zappatore[3]

[1] ENEA, Via Enrico Fermi 45, 00044 Frascati, Rome, Italy
[2] École Polytechnique Fédérale de Lausanne (EPFL), Swiss Plasma Center (SPC), 5232 Villigen PSI, Switzerland
[3] NEMO Group, Dipartimento Energia, Politecnico di Torino, Corso Duca degli Abruzzi 24, Torino, Italy
[4] DTT S. c. a r. l., Via Enrico Fermi 45, 00044 Frascati, Rome, Italy

E-mail: gianluca.demarzi@enea.it

Keywords: SULTAN tests, AC losses, poloidal field coils, NbTi conductors, current-sharing temperature, minimum quench energy, superconducting fusion magnets

OPEN ACCESS

RECEIVED
3 January 2025

REVISED
14 February 2025

ACCEPTED FOR PUBLICATION
5 March 2025

PUBLISHED
18 March 2025

Original content from this work may be used under the terms of the Creative Commons Attribution 4.0 licence.

Any further distribution of this work must maintain attribution to the author(s) and the title of the work, journal citation and DOI.

Abstract

The poloidal field (PF) magnet system of the Divertor Tokamak Test (DTT) facility consists of 6 superconducting coils with full top-down symmetry, realized in Nb_3Sn (PF1 and PF6) and NbTi (PF2, PF3, PF4 and PF5). To validate the NbTi PF coil design, short samples of the cable-in-conduit-conductor cables (CICCs) have been qualified by dedicated cryogenic tests in the SULTAN facility at Swiss Plasma Centre (SPC, EPFL). In this work, we present the results of the two test campaigns conducted in August and September 2022, for the PF2/5 and PF3/4, respectively. The extensive characterization of the NbTi PF samples included a set of AC loss measurements using bipolar sinusoidal pulsing, as well as a set of DC tests spanning the range of the coils operability to assess the critical current, I_c, and the current sharing temperature, T_{cs}. The performances have been checked after electro-magnetic (EM) cyclic loading (up to 1000 cycles) at different B/I loads. The minimum quench energy (MQE) has also been measured at different temperatures. All tests confirmed the effectiveness of the PF CICCs design, showing good performance above the minimum acceptance values even at currents 110% higher than the nominal value.

1. Introduction

The Divertor Tokamak Test (DTT) facility [1, 2] is currently undergoing construction at the ENEA Research Center in Frascati, as part of the European Roadmap to the Realisation of Fusion Energy [3, 4]. It aims to advance nuclear fusion technology by tackling pivotal issues related to the divertor system and optimizing power exhaust management.

The DTT facility will feature six Poloidal Field (PF) coils, symmetrically arranged about the equatorial plane and forming geometrically identical pairs (*i.e.*, PF1 and PF6 share almost identical geometry, as do PF2/PF5 and PF3/PF4). These coils will be independently powered and constructed using superconducting Cable-In-Conduit Conductors (CICCs) configured in double and/or quadri- pancakes, similar to the designs employed in ITER [5], JT-60SA [6], and the prospective EU DEMO [7]. Together with the CS coil, they provide the 16.4 Wb flux for the plasma initiation at breakdown. Due to the demanding magnetic requirements (B_{max}) on the uppermost and lowermost PF coils, PF1 and PF6, utilize Nb_3Sn superconducting material, whereas the remaining PF coils (PF2/5 and PF3/4) rely on NbTi. The layout of the NbTi CICC conductors and the corresponding design choices are detailed in [8–10] and summarized in figure 1 and table 1.

The TF conductors have been successfully tested in SULTAN, and they meet the design requirements [11]. In this work, we will present and analyze the results of two experimental campaigns conducted during August and September 2022 in the SULTAN facility for the PF2/5 an PF3/4, at the Swiss Plasma Center (SPC) of the École Polytechnique Fédérale de Lausanne (EPFL), in Villigen, Switzerland. These campaigns were intended to validate the design choices comprehensively, and to assess the AC losses they may undergo in operation. The

© 2025 The Author(s). Published by IOP Publishing Ltd

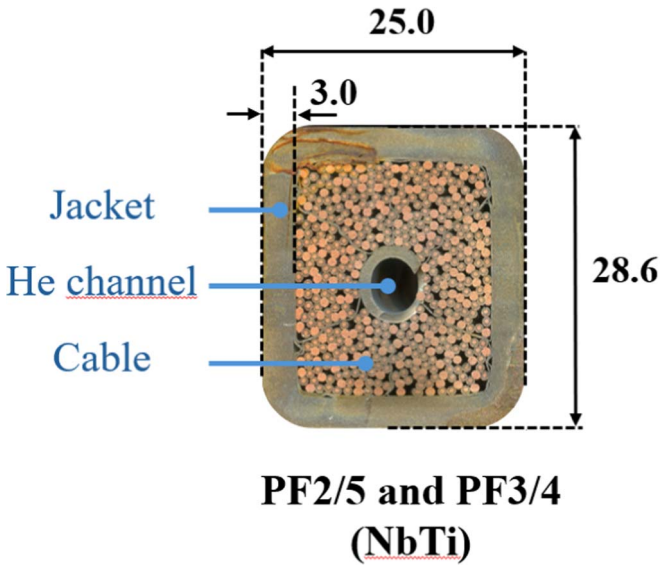


Figure 1. The cross-section of the NbTi PF2/5 and PF3/4 CICCs.

Table 1. DTT PF CICC parameters.

Parameter	Units	PF2/5	PF3/4
SC/Cu strands	—	162/324	324/162
Void fraction	%	28	28
Turn insulation	mm	1.4	1.4
Conductor height	mm	28.6	28.6
Conductor width	mm	25.0	25.0
Jacket thickness	mm	3.0	3.0
Twist pitch sequence	mm	35/80/125/190/290	35/80/125/190/290
Cable pattern	—	(1SC+2Cu) × 3 × 3 × 3 × 6	(2SC+1Cu) × 3 × 3 × 3 × 6
$I_{op,\max}$	kA	27.1	28.6
$B_{\max}$	T	4.2	5.3
ΔT_m	K	1.9	1.7
T_{op}	K	4.5	4.5

testing program was dictated by the operating mode of the PF magnets. The present paper, after a brief overview of the superconducting properties of the constituting NbTi strand, of the DTT PF SULTAN samples and of the adopted testing instrumentation, provides a thorough description of the test outcomes and data analysis of both SULTAN samples.

After presenting DC tests results, particular emphasis has been given on AC losses and stability measurements, which are significant in pulsed magnets like the DTT PFs.

2. Parameterization of the critical surface of the Furukawa NbTi strand

The superconducting NbTi strands have been designed and manufactured by Furukawa Electric Co, Ltd (FEC) and are characterized by a diameter of 0.82 mm, a Cu:non-Cu > 1.92 and a critical current density I_c(4.2 K, 5 T) > 500 A. The main parameters of the NbTi strand are reported in table 2.

The critical surface of the NbTi strand has been explored in a wide *B*-*T* range by means of transport and inductive measurements.

Direct transport critical current measurements, $I_c(B,T)$, have been performed using the ENEA Variable Temperature Insert (VTI) test facility, with a transverse external field up to 10 T. A warm hole of 47 mm diameter allows to insert a sample wound on a stainless steel cylindrical barrel for transverse field measurement of wires. The temperature of the sample is regulated by helium gas flow, pumped through a needle-valve from the same LHe bath of the background field superconducting coil.

Magnetization measurements have been carried out using a Vibrating Sample Magnetometer (VSM) by Oxford Instruments, capable of operating with magnetic fields up to 12 T, and at variable temperatures,

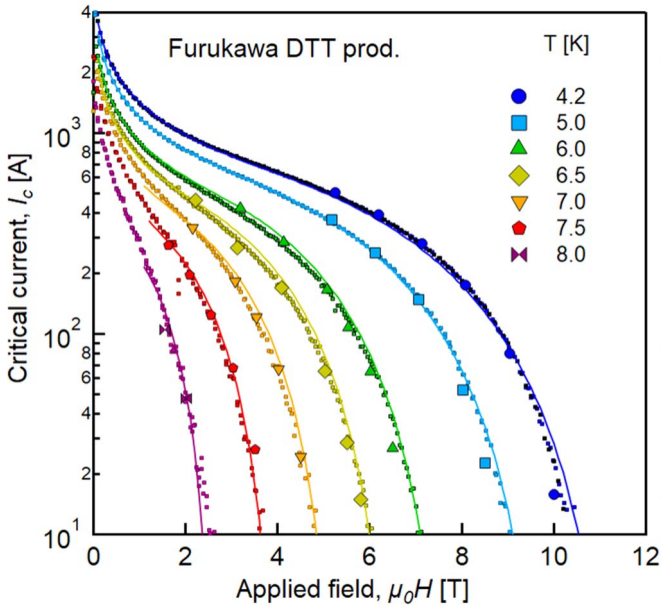


Figure 2. Critical current of the NbTi Furukawa strand as a function of an applied magnetic field, at different temperature from 4.2 K to 8.0 K. Data have been collected by transport (markers) and inductive methods (small square symbols). Lines represent the fit to the two-component model for the NbTi critical surface [14].

Table 2. Main parameters of the NbTi strand.

Ni-coated NbTi strand	Units	Value
Ni-coating	mm	1.5 ± 0.5
Diameter w/ Ni-coating	mm	0.820 ± 0.005
Diameter wo/ Ni-coating	mm	0.817 ± 0.003
# filaments		1914
Filament diameter	μm	11
Effective diameter	μm	12
Cu:nonCu ratio		>1.92
Twist pitch	mm	15 ± 2
I_c(4.2 K, 5 T)	A	>500
RRR		>120

obtained through a controlled helium gas flow. Magnetization measurements extend the critical current determination to lower fields and are used to determine characteristic parameters, like the effective filament diameter, d_{eff}, a useful parameter for the estimation of AC losses.

The strand's critical currents have been extracted from the magnetization loops using the Bean Model [12, 13]. For cylindrical samples positioned perpendicularly to the magnetic field, the following expression is used:

$$I_c(B,\ T) = \frac{3\pi}{4}\frac{\Delta m(B,\ T)}{d_{eff}}\frac{1}{L} \tag{1}$$

where Δm is the magnetic moment difference between the positive and the negative branches of the hysteresis loop, whereas L is the length of the measured sample.

Figure 2 presents both DC transport and inductive measurements performed at different temperatures ranging from 4.2 K to 14 K. To enable a meaningful comparison between transport and magnetization data, it is essential to account for the self-field generated by the transport current, which is absent in inductive measurements. Consequently, in figure 2 the transport I_c are plotted as a function of the peak field, defined as the sum of the applied field (B_a) and the maximum self-field (B_{sf}) experienced by the strand. B_{sf} can be estimated using the Biot–Savart law: $B_{sf} = \mu_0 I_s/(2\pi r_f)$, where I_s is the strand's transport current, and $r_f = 0.33$ mm is the radius of the filamentary zone in the strand cross-section.

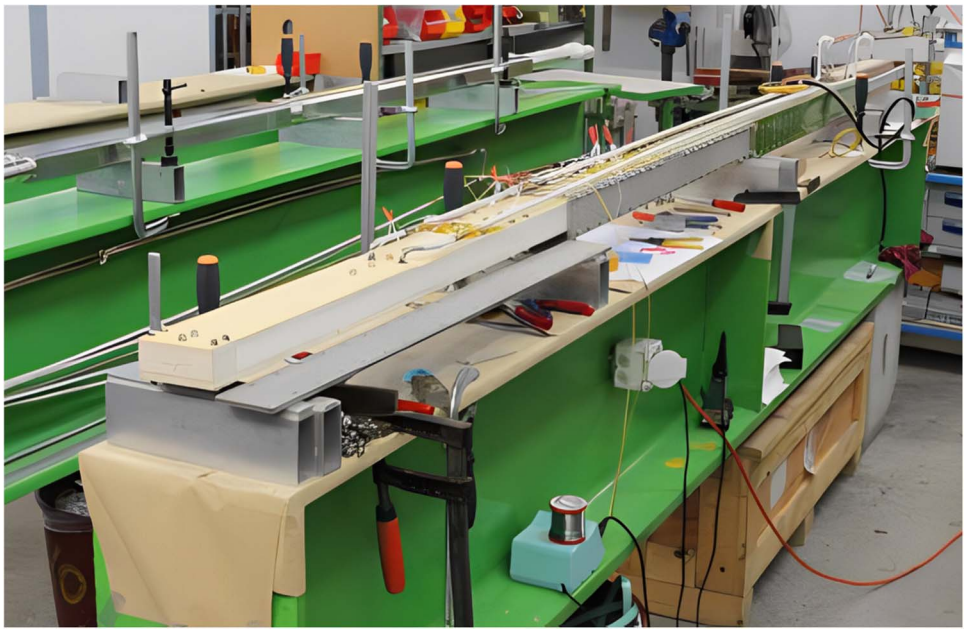


Figure 3. View of the SULTAN Sample PF2/5 on the bench.

Table 3. Parameters of the two-components model [14] for the critical surface of the Furukawa NbTi strand, DTT-PF production.

Parameters	Units	Value
C_0	kA·T·mm^{-2}	32.59
T_c	K	8.93
B_{c20}	T	15.79
δ	—	0.65
α_1	—	2.07
β_1	—	2.32
α_2	—	0.71
β_2	—	5.27
γ	—	1.64
n	—	1.7

The comparison of the results obtained from inductive and transport measurements enabled us to determine an effective filament diameter ($d_{eff} = 12\,\mu m$), that is in very good agreement with the value of the geometrical filament size ($d_{geom} = 11\,\mu m$).

The experimental data of figure 2 have been analyzed using the two-component model [14], which, compared to the conventional formula for the NbTi critical surface [15], is valid over a wider range of field and temperature.

The fitting parameters have been obtained using a global analysis tool by Wavemetrics Igor Pro®, which allows to fit multiple data sets in a single curve fit. The set of fitting parameters is reported in table 3.

3. The DTT PF2/5 and PF3/4 SULTAN samples

The main parameters of the DTT PF CICCs are shown in table 1 and their cross-sections are reported in figure 1. The two SULTAN samples were assembled at EPFL-SPC, and hereafter will be referred to as 'Sample PF2/5' and 'Sample PF3/4'. Each sample is comprised of two identical straight CICC sections joined at the bottom, referred to as *legs*. Figure 3 shows a view of the Sample PF2/5 on the bench.

In the SULTAN test facility, the two legs were joined at the bottom and electrically connected at the top to the SULTAN superconducting transformer.

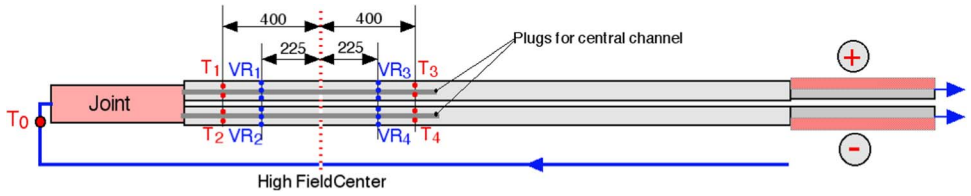


Figure 4. Instrumentation scheme of the SULTAN PF samples. The voltage taps, VR1–4, and the temperature sensors, T1–4, are located in the high field zone.

According to the conventional nomenclature, in the following sections we will refer to the left leg as PF-A and the right leg as PF-B. The samples were vertically placed within the magnet bore. A clamping mechanism maintained the parallel alignment of the two legs, counteracting the electromagnetic (EM) loads.

The SULTAN background magnetic field was applied to a segment of the conductor approximately 0.45 meters in length (here referred to as the high field zone, HFZ). The inductive AC coil was positioned in correspondence of the HFZ. The bottom joint enabled both legs to be powered by a single power supply, thus allowing simultaneous testing of the two conductors. The assembly of the two legs ensured that the EM load was applied to the wider side of the conductor. Cooling was achieved via a forced flow of supercritical helium circulating from the bottom joint to the upper terminations, flowing concurrently through both legs.

4. Sample instrumentation and test program

The conductors of both samples PF2/5 and PF3/4 are equipped with temperature (T), voltage (V), mass flow rate (dm/dt) and pressure (P) sensors distributed along their length, as depicted in the instrumentation layout illustrated in figure 4, identified with a specific standard nomenclature used in SULTAN. Temperature probes and voltage taps are mounted on the conductor's jacket. Each PF leg is equipped with four voltage tap pairs (VH) and two temperature sensor (T1, T3 and T2, T4 for the PF-A and PF-B, respectively) across the HFZ: each pair consist of four distinct sensors, positioned on each side of the jacket at the same axial location. Additional voltage taps and thermometers were deployed at the bottom joint, the whole sample and the terminals, respectively.

The cryogenic tests conducted in SULTAN involved cable characterizations under relevant close-to-operative conditions. To remain conservative, during the design phase, it was decided to size the cables to withstand a maximum current equal to 110% of the maximum operative current reached during a plasma scenario ($I_{op,max}$ in table 1). Consequently, these choices are reflected in the test programs.

For both samples, the test program consists of the following main characterizations:

- AC losses before electromagnetic (EM) loading, to evaluate the heat loads during the various plasma scenarios. AC losses characterizations have been carried out using sinusoidal AC cycles (up to a frequency of about 10 Hz);
- DC tests: current-sharing temperature, T_{cs}, and critical current, I_c, measured at $T_{cs} + 0.4$ K, to assess the minimum temperature margin, ΔT_m, an important design parameter reported in table 1. In SULTAN, I_c measurements are typically performed at a temperature of $T_{cs} + 0.4$ K because this ensures that the critical electric field ($E_c = 0.1$ μV cm^{-1}) is sufficiently exceeded to allow for an accurate n-value fitting;
- AC losses after 1000 EM loading (from 0 to B_{max}, after 50, 150 and 1000 cycles), to compare with AC losses results before EM lcycling;
- Stability tests: measurements of the Minimum Quench Energy (MQE), to verify that the PF conductors are stable against transient electromagnetic disturbances.

Additionally, few more I_c and/or T_{cs} tests at different sample current and background field values have been performed, in order to reconstruct a wide CICC operation space and verify the quench field values, as discussed later.

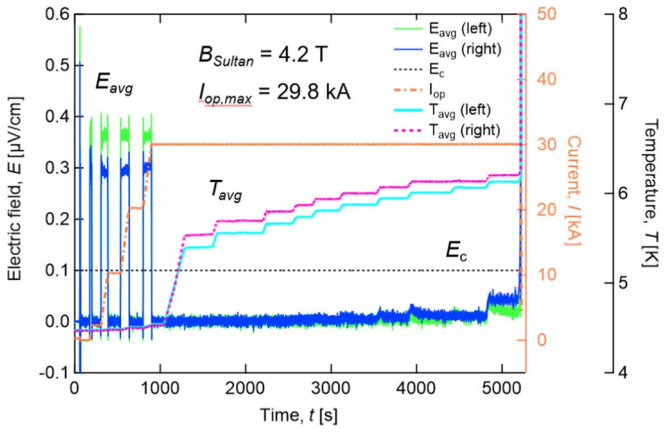


Figure 5. Current (orange dash-dotted line), average electric field, E_{avg}, over the crown array of voltage taps across the HFZ (PF-A: green line; PF-B: blue line) and average temperatures, T_{avg}, at the HFZ (PF-A: purple dashed line; PF-B: cyan continuous line) plotted as a function of time during a T_{cs} run performed on sample PF2/5. The dotted line represent the electric-field criterion threshold.

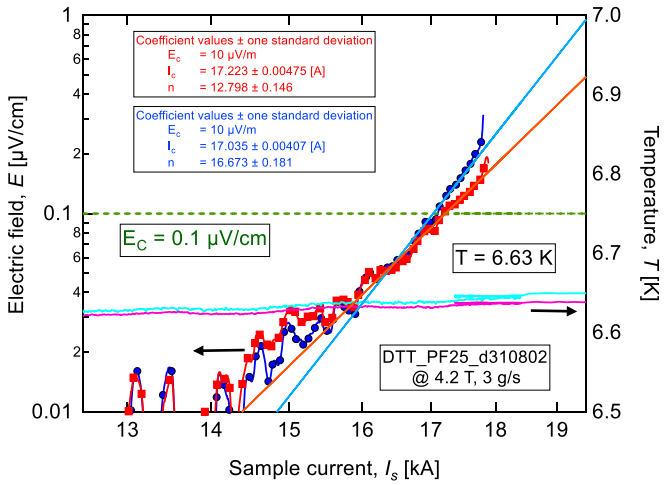


Figure 6. Average electric field over the crown array of voltage taps across the HFZ (PF-A: red squares; PF-B: blue circles) and average temperature at the HFZ (PF-A: purple line; PF-B: cyan line) plotted as a function of sample current, I_s, during a I_c run performed on sample PF2/5. The dashed line represent the electric-field criterion threshold. The I_c measurements in SULTAN are usually performed at a temperature corresponding to $T_{cs} + 0.4$ K, to guarantee the I_c assessment within the measurement.

5. DC test results in SULTAN

The DC performance of the conductor is assessed through T_{cs} and I_c tests. These measurements have been conducted in separate tests before and after EM cyclic loading.

The measurement of the current sharing temperature, at a given operating current and field, is one of the key tests for the qualification of the DTT PF conductors.

The T_{cs} is evaluated by means of the voltmetric method based on the evaluation of the voltage drop measured along the HFZ [16]. A detailed description of the analysis procedures for SULTAN DC and AC measurements can be found in [17, 18]. T_{cs} is measured at constant backgound field and current, by slowly raising in small steps the operating temperature until a voltage builds up at the high-field zone. The average signal of the crown of voltage taps located around the jacket is taken to measure the voltage development over the HFZ [18]. From the reversible voltage-temperature transition, the measured T_{cs} at 10 μV m^{-1} is compared with the requirement of the design, as illustrated in figure 5 as an example.

The I_c tests are performed at a temperature corresponding to ($T_{cs} + 0.4$ K) and measuring the electric field during the current ramp up to quench. A typical run is shown in figure 6.

For T_{cs}/I_c evaluations, the average of different voltage signals across the HFZ was considered, as a function of the average temperature between all sensors installed immediately downstream and upstream of the HFZ. The difference among the different voltage pairs has been observed to be negligible.

To compare the performance of the PF2/5 and PF3/4 conductors with those of their individual strands, we have developed a methodology to evaluate strand performance under the conductors' test conditions.

This procedure enables the assessment of cable performance using 2D field maps corresponding to each combination of background magnetic flux density and transport current. The 2D maps describe the magnetic flux density in the sample cross-sections at the center of the HFZ, assuming a uniform current distribution across the cross-sections.

To describe the DC performance of the conductors based on the properties of the constituting strands, it is useful to define an effective field, B_{eff}, in such a way that [19]:

$$I_c^{cable} \cong N I_c^{strand}(B_{eff}) \tag{2}$$

$$B_{eff} = B_{SULTAN} + k_{eff} I_c^{cable} \tag{3}$$

where N is the number of the strands, and k_{eff} is the self-field factor. The effective self-field includes the field generated by both conductors.

To compute the effective field, and hence k_{eff}, acting on the conductor pair, a 2D finite element model of the SULTAN sample section has been implemented by means of the *magnetic field* interface of the commercial software Comsol Multiphysics® [20].

The average electric field, $\langle E \rangle$, on the conductor sections is given by the following formula:

$$\langle E \rangle = E_c \iint \left(\frac{I_{op}}{I_c(B_{eff},\ T_{cs})} \right)^n dx\, dy \tag{4}$$

where the surface integral is performed on the entire section of the conductors, $B = B(x,y)$ is the local value of the magnetic field to be included in the parameterization of the critical surface of the NbTi strand, discussed in section 2, and n is the n-index value, characterizing the steepness of the *Electric Field versus Sample Current* transition of the constituting strands.

In (4), B_{eff} is chosen such that the average electric field over the sample cross-section equals the specific electric field criterion $E_c = 10\ \mu V\ m^{-1}$.

5.1. DC tests, sample PF2/5

The minimum expected T_{CS}, *i.e.* the PF 2/5 coil design acceptance criterion, is defined as $T_{op} + \Delta_m = 6.4$ K (see table 1) at 110% of the maximum operative current, $I_{op,\max}$ (29.8 kA), and under a peak field of 4.2 T. In SULTAN DC tests, we used a background field of 4.2 T, corresponding to a maximum field of about 4.85 T at 29.8 kA.

To be specific, the series of DC tests included:

- T_{cs} at 4.2 T/29.8 kA with intermediate EM cycles (50, 150, 1000) at 4.2 T/29.8 kA;
- I_c at 4.2 T/T_{cs}+0.4 K before and after EM cycling loads;
- T_{cs} test at 33.0 kA. This last test has been performed at a further 10% extra current to check the robustness of the design.

In figure 7, the results of the DC tests are summarized. The I_c data appears on the left side of the graph (around 17 kA), whereas the T_{cs} data are positioned on the right side (at 29.8 kA and 33.0 kA). The performance of the sample, assessed using the two-component model for the constituting strand [14], is plotted in figure 7 as a continuous line. Equation (2), combined with the appropriate k_{eff} factor and the two-component model, is indeed capable of accurately reproducing the experimental data.

Moreover, we observe a slight decrease in DC performance after cyclic loading.

The expected design performance at SULTAN test conditions, which are represented by a dashed line in figure 7, is found to be well below the measured performance of the sample, thus confirming the goodness of the design.

5.2. DC tests, sample 3/4

The PF 3/4 coil design acceptance criterion is $T_{op} + \Delta_m = 6.3$ K (see table 1) at 110% of the maximum operative current, $I_{op,\max}$ (31.5 kA), and under a peak field of 5.3 T.

The series of DC tests included:

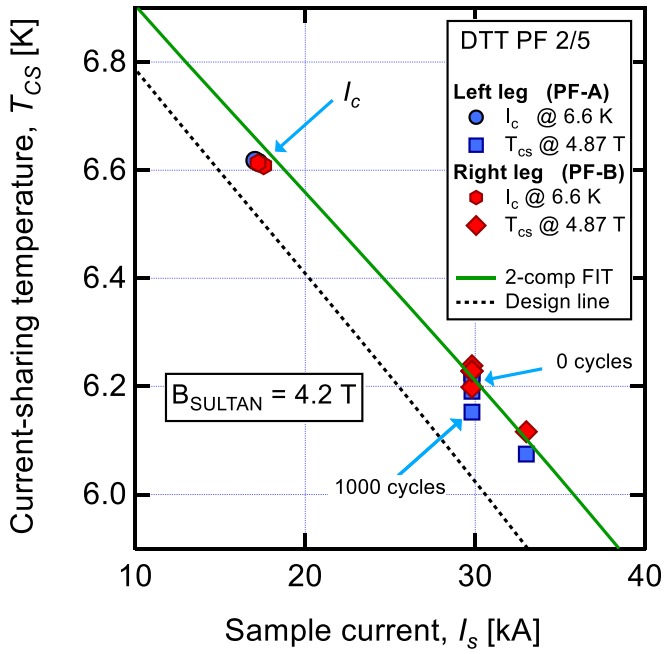


Figure 7. Sample PF2/5: the DC tests as a function of sample current (markers). The continuous line represents the fit obtained using the two-component model [14], whereas the dashed line represents the design line.

- T_{cs} at 5.3 T/31.5 kA with intermediate EM loading (1000 cycles) at 5.3 T/31.5 kA;
- I_c at 5.3 T/T_{cs}+0.4 K before and after EM cycling;
- T_{cs} test at 5.3 T/28.6 kA, 4.64 T/28.6 kA, 4.64 T/25.0 kA, and 5.3 T/25.0 kA.

DC tests results for PF3/4 SULTAN sample are presented in figure 8. For this sample, it is observed a limited current sharing regime with quench occurring sometimes below the nominal 10 μV m^{-1} criterion. Specifically, when both legs were heated at the same rate, the left leg quenched slightly earlier. Nonetheless, a slow approach to thermal runaway was attempted, with temperature increments of 0.15–0.25 K approaching quench. In instances where the electric field did not reach the 10 μV m^{-1} criterion, small-range extrapolations were often employed to determine the $T_{cs}T_{cs}$ value.

In all those cases where this was not possible, the quench temperature, T_q, was considered in place of T_{cs}.

In figure 8, both DC measurements carried out at B_{peak} = 6.0 T (B_{SULTAN} = 5.3 T) and at B_{peak} = 5.3 T (B_{SULTAN} = 4.64 T) are presented; the 5.3 T/31.5 kA design line is represented by a dashed curve.

To describe the conductor performance, we use again equations (2)–(3). However, and differently from what observed for Sample PF2/5, the effective field in this case practically coincide with the peak field on the conductor. In other words, the conductor performance is obtained extrapolating the strand performance subjected to a uniform peak field, corresponding to the peak field on the conductor (see figure 9).

The different behavior of the two samples, PF2/5 and PF3/4, can be explained considering the higher gradient of the magnetic field on the PF3/4 sample, especially at the higher current 31.5 kA, leading to larger peak electric fields on the high-field side of the cross section. This, in turn, accounts for the limited current-sharing regime [19, 21] observed in Sample PF3/4, which is absent in Sample 2/5.

Similarly to Sample PF2/5, a slight decrease in DC performance after cyclic loading is found; also, the expected design line of Sample PF3/4 under SULTAN test conditions is lower compared to the experimental DC data, thus confirming the robustness of the design.

6. AC test results in SULTAN

A set of AC loss measurements has been conducted on the sample virgin state (before any Lorentz forces loading), with a 2 T background DC field and zero operating current before and after EM cyclic loading, using

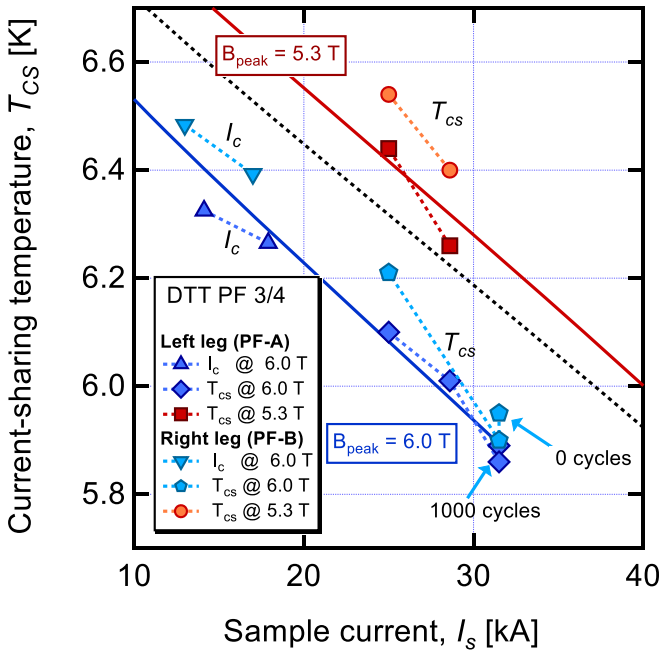


Figure 8. Sample PF3/4: the DC tests as a function of sample current, at $B_{peak} = 6.0$ T ($B_{SULTAN} = 5.3$ T) and $B_{peak} = 5.3$ T ($B_{SULTAN} = 4.64$ T). The continuous lines represent the fits obtained at their corresponding fields using the two-component model [14], whereas the dashed line represents the 5.3 T/31.5 kA design line. The experimental data obtained by means of *Ic* and T_{cs} measurements at the same background magnetic field are connected with dashed lines and labelled with 'I_c' and 'T_{cs}' tags, respectively.

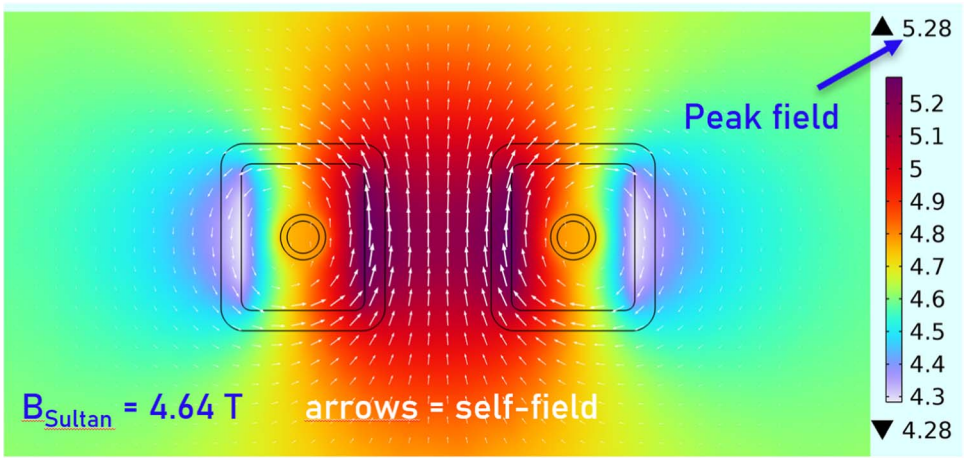


Figure 9. Sample 3/4: the magnetic field map at $I_{op} = 31.5$ kA. White arrows represent the self-field component, which adds to the background SULTAN field ($B_{SULTAN} = 4.64$ T, directed along the *y*-axis). The peak file on the conductor ($B_{peak} = 5.28$ T) is located on the conductors' regions closer to the center of the sample.

sinusoidal pulsing at different frequency of excitation (0.1 to 10 Hz). A series of runs was also carried out at different background field and operating currents after 1000 EM loading cycles, in order to evaluate their effect on the AC behaviour of the cables.

AC losses have been assessed by using a calorimetric method:

$$Q_{AC} = \frac{\dot{m}}{\nu} \quad (h_{flat-top} - h_{offset}) \tag{5}$$

where ν is the frequency, $\dot{m}$ is the mass flow rate, and h_{offset} ($h_{flat\text{-}top}$) is the Helium enthalpy computed at a given initial (final) temperature and pressure.

An example of the temperature, output pressure and mass flow rate used to compute the loss with (5) is reported in figure 10 for Sample 2/5, right leg ($B_{SULTAN} = 2$ T, $B_{AC} = \pm 0.2$ T, $\nu = 0.4$ Hz).

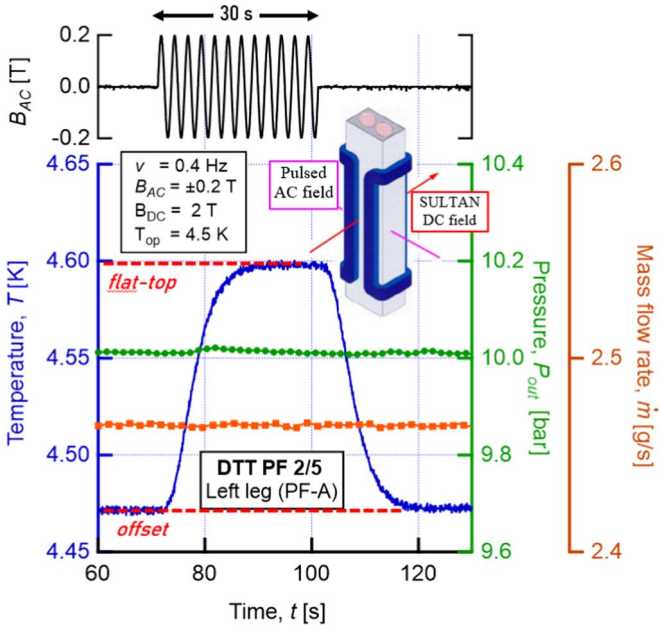


Figure 10. PF2/5, left leg: the temperature (blue continuous line), outlet pressure (green circles), and mass flow rate (orange squares) recorded as a function of time. A 0.4 Hz sinusoidal pulsing is applied for 30 s (top graph), producing an AC field with amplitude $B_{AC} = \pm 0.2$ T. The AC field, applied to the HFZ, is perpendicular to the SULTAN background field. The AC loss, Q_{AC}, is calculated using the henthalpy values $h_{offset} = h(4.47\,\text{K}, 10.0\,\text{bar})$ and $h_{offset} = h(4.59\,\text{k}, 10.0\,\text{bar})$, and $\dot{m} = 2.47\,\text{g}\,\text{s}^{-1}$.

6.1. AC tests, sample 2/5

The series of tests included AC loss measurements at:

- 2 T/0 kA, before and after EM cycling;
- 4.2 T/0 kA and 4.2 T/29.8 kA, after EM cycling.

The total energy density deposited per cycle, computed from the calorimetric measurements for Sample 2/5, is plotted in figure 11 as a function of the frequency of the AC field generated by the SULTAN AC coils. The conductor exhibits an increasing AC loss with frequency without reaching a peak or plateau, both before and after EM cycles, in the investigated range (<10 Hz).

Furthermore, there is a notable decrease in AC loss at each measured frequency value, when the amplitude of the magnetic flux density is raised from 2 T to 4.2 T.

This reduction primarily arises from the *magnetoresistance* of the copper, which increases with higher applied magnetic fields, consequently diminishing coupling losses.

This behaviour has also been observed for the NbTi conductors of the ITER project, namely PF5CN3, PF2CN4, CBCN2, and CCCN3 conductors [18].

Although the addition of a transport current should, in principle, enhance the losses in multifilamentary strands [22], an actual CICC may behave differently. In facts, and as observed in figure 11, the AC losses decrease in the presence of a transport current for both conductor legs. This behavior is similar to that of the JT60-SA Toroidal Field conductor reference sample [23], which has a similar layout except for the absence of a central channel.

It is well established that in multi-stage CICCs, the different transverse resistances of the cable stages lead to the presence of multiple time constants, as described in [22, 24]. These time constants are determined by multiple induced current loops. Each time constant is pertinent to a specific frequency range, and typically, several time constants are required to accurately fit the loss versus frequency curve. However, when a transient AC loss regime predominates, a single time constant, denoted as $n\tau$, can adequately describe the experimental data. In this practical approach, $n\tau$ is experimentally determined from the initial slope of the loss curve. The simplified expression of the AC loss versus frequency, which disregards any screening effects, is of the form:

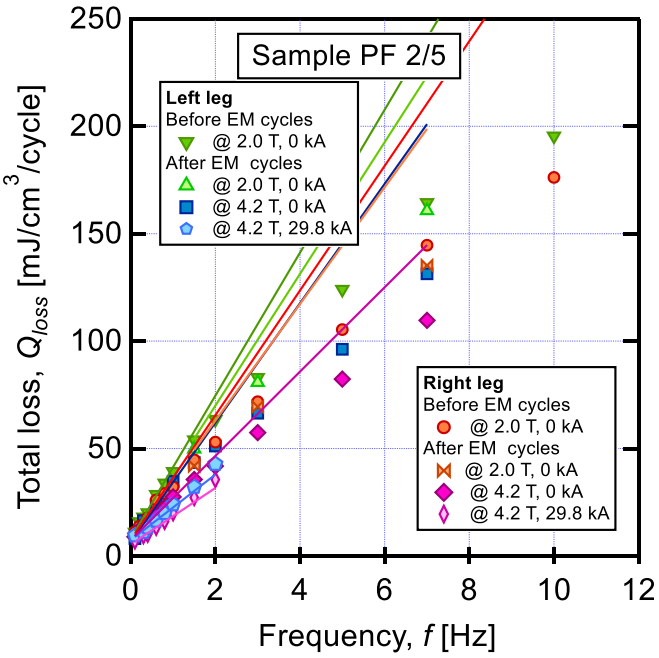


Figure 11. Ac loss versus frequency curve of Sample PF 2/5 at 2 T and 4.2 T SULTAN background field, *w/wo* DC tranport current, and before/after the EM cyclic loading. Cycles performed with $B_{AC} = \pm 0.2$ T amplitude.

Table 4. Time constant values of Sample PF2/5 before and after EM cycles, at different field and current combinations.

Test sequence, sample PF2/5	$n\tau$ [ms] PF-A	$n\tau$ [ms] PF-B
Before EM cycles, 2 T/0 kA	53	46
After EM cycles, 2 T/0 kA	49	43
After EM cycles, 4.2 T/0 kA	44	31
After EM cycles, 4.2 T/29.8 kA	24	21

$$Q_{loss} = Q_{hyst} + \frac{B_{AC}^2 \pi \omega}{\mu_0} n\tau \tag{6}$$

In (6), Q_{hyst} represents the hysteresis loss in the zero frequency limit.

In figure 11, lines represent fits obtained in the range 0.1–0.8 Hz using the single time constant approximation of equation (6). The results are reported in table 4. Coupling time constant values of 49.7 ms and 39.6 ms were obtained for the 'PF-A' and 'PF-B' losses on virgin samples, respectively.

The effect of the EM cycling is to slightly decrease the $n\tau$ values. Moreover, increasing the magnetic field causes an increase in effective resistivity due to the magnetoresistance effect, resulting in a decrease in $n\tau$.

6.2. AC tests, sample 3/4

The series of tests included AC loss measurements at:

- 2 T/0 kA, before and after EM cycling;
- 5.3 T/0 kA and 5.3 T/31.5 kA, after EM cycling.

The total energy density deposited per cycle of Sample 3/4 is depicted in figure 12 as a function of the frequency. Similar to the results of Sample 2/5, this conductor shows an increasing AC loss with frequency, without reaching a peak or plateau, both prior to and following EM cycles.

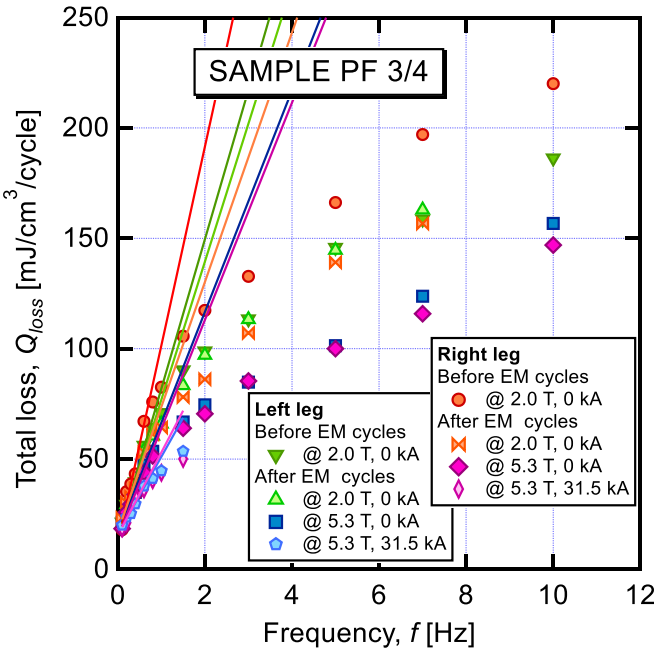


Figure 12. Ac loss versus frequency curve of Sample PF 3/4 at 2.0 T and 5.3 T SULTAN background field, *w/wo* DC tranport current, and before/after the EM cyclic loading. Cycles performed with $B_{AC} = \pm 0.2$ T amplitude.

Table 5. Time constant values of Sample PF3/4 before and after EM cycles, at different field and current combinations.

Test sequence, sample PF3/4	$n\tau$ [ms] PF-A	$n\tau$ [ms] PF-B
Before EM cycles, 2 T/0 kA	108	143
After EM cycles, 2 T/0 kA	99	90
After EM cycles, 5.3 T/0 kA	80	78
After EM cycles, 5.3T/ 31.5 kA	56	60

Furthermore, there is a decrease in AC loss across the entire frequency measurement range when a DC transport current is applied, or when the amplitude of the magnetic flux density is increased from 2 T to 5.3 T, while the effect of EM cycling loading is negligible.

In figure 12, lines represent fits obtained in the range 0.1–0.8 Hz. The results of the fits of equation (6) to the experimental data are reported in table 5.

The behavior of the AC loss curves in the presence of a higher background field, and *w/wo* transport current, qualitatively resembles that of Sample 2/5. Quantitatively, the losses in Sample PF3/4 are greater than those in Sample PF2/5 because the former contains twice the number of superconducting strands, and the losses are normalized to the total volume. This is reflected in the $n\tau$ values reported in tables 4 and 5.

Finally, it is noteworthy that Sample 3/4 has an identical number of NbTi strands and segregated copper as the JT60-SA conductor [23].

6.3. Discussion on the EM cycling and AC losses

Losses in both samples and legs are reduced by cycling, due to the expected increase in transverse resistance. This also leads to the slight reduction in $n\tau$ observed after the EM loading cycles.

Comparable with Cr-plated Nb_3Sn strands, bare copper or coated NbTi strands, without severe reaction heat treatment, also exhibit a strong effect related to transverse cable loading [25]. In other words, AC loss in the NbTi CICCs usually decreases after the conductor undergoes electromagnetic cycling. For example, in [26] the experimental $n\tau$ values of the eight samples from the prototype full-size ITER Model Coil NbTi have been measured as a function of transverse loading using a press up to 40,000 cycles, to simulate the effect of the Lorentz forces. A consistent correlation is found between the experimental AC loss and interstrand contact resistance (R_c) results. The authors also observed a strong impact of cyclic loading on the AC loss and *Rc*, which may change by orders of magnitude. The strand-to-strand micro-sliding, induced by electromagnetic forces, leads to changes in the interstrand and interbundle R_c, typically ranging from one to two orders of magnitude

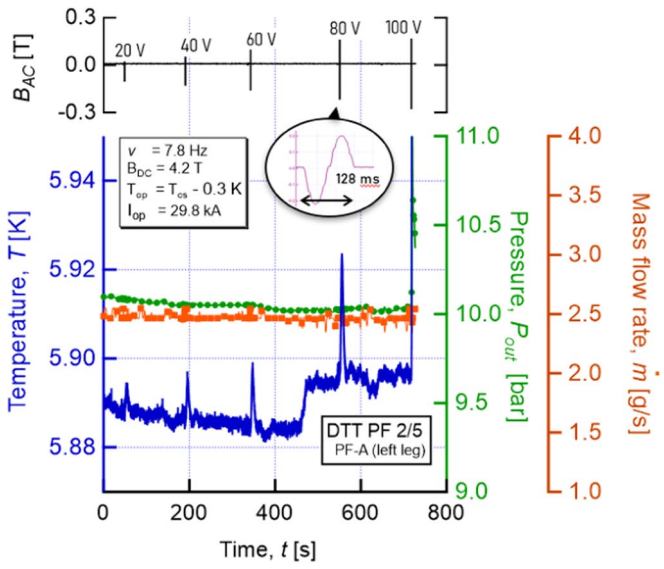


Figure 13. PF2/5, left leg: the temperature (blue continuous line), outlet pressure (green circles), and mass flow rate (orange squares) recorded as a function of time during an MQE run at $T = T_{cs} - 0.3$ K, $B_{DC} = 4.2$ T, and $I_{op} = 29.8$ K. A 128 ms sinusoidal pulsing is applied for one period (top graph). Each peak corresponds to a magnetic field pulse of the AC coils with increasing B_{AC} amplitude.

depending on the surface coating or internal barrier of the strand. For the ITER NbTi CICCS, it was observed that the increase in R_c with cycling is strongly correlated with the allowed degree of cable compression and/or relaxation. In other words, the decrease in coupling loss with magnet loading appears to be strongly correlated with the void fraction of the conductor. It is plausible that similar phenomena occur in the PF conductors of DTT.

The reductions in $n\tau$ are comparable to those obtained for the ITER PF conductors [26]. The mitigation of AC loss due to this 'cyclic loading effect' in the PF conductors is beneficial for the DTT magnet operation.

7. Stability tests

Minimum Quench Energy (MQE) tests constitute a crucial parameter for assessing conductor performance. MQE tests were conducted at the conclusion of the test campaigns, after 1000 electromagnetic (EM) cycles, by injecting power into the conductor through the Joule losses of currents induced in the sample by flux density variations.

This was achieved using sinusoidal pulses with increasing amplitude until a quench was triggered (see figure 13).

Regarding Sample PF2/5, MQE tests were conducted at 4.2 T background field, without sample current ('calibration' runs) and with a sample current of 29.8 kA, at 2.5 g s^{-1} helium mass flow rate. MQE was measured at two distinct temperatures: $T_{cs} - 0.1$ K and $T_{cs} - 0.3$ K. The calibration run, was performed at $T_{cs} - 0.3$ K.

Concerning Sample PF3/4, MQE tests were performed at 5.3 T background field, with a sample current of 31.5 kA, with a mass flow rate of 2.5 g s^{-1}. Calibration runs were recorded at T_{cs}–0.1 K, whereas MQE was measured at three distinct temperatures: $T_{cs} - 0.1$ K, $T_{cs} - 0.3$ K, and $T_{cs} - 0.5$ K.

An example of calorimetric measurement is illustrated in figure 13. The methodology employed to assess the quench energy closely resembles the approach outlined earlier for the measurement of AC losses. The total energy is deposited to the cable during a 128 ms sinusoidal pulse of magnetic flux density, with variable amplitude, generated by the AC coils. The energy deposited was calculated for both legs for the 'calibration' run and for the current runs without quenching, using calorimetry according to equation (7):

$$Q_{dep} = \dot{m}(t_i) \int_{t_i}^{t_f} [h(t) - h_0] dt \tag{7}$$

where Q_{dep} is the energy deposited, $\dot{m}(t_i)$ is the mass flow rate in each conductor evaluated before the pulse, $h(t)$ is the helium enthalpy as function of time, evaluated from the standard He properties library [27], and h_0 is an offset averaged value of the enthalpy evaluated on a stabilized time-interval before the inductive coil discharge.

The MQE test results are plotted in figures 14, 15 for Sample PF2/5 and Sample 3/4, respectively. The energy density deployed to the conductor during each pulse is plotted as a function of the peak AC field.

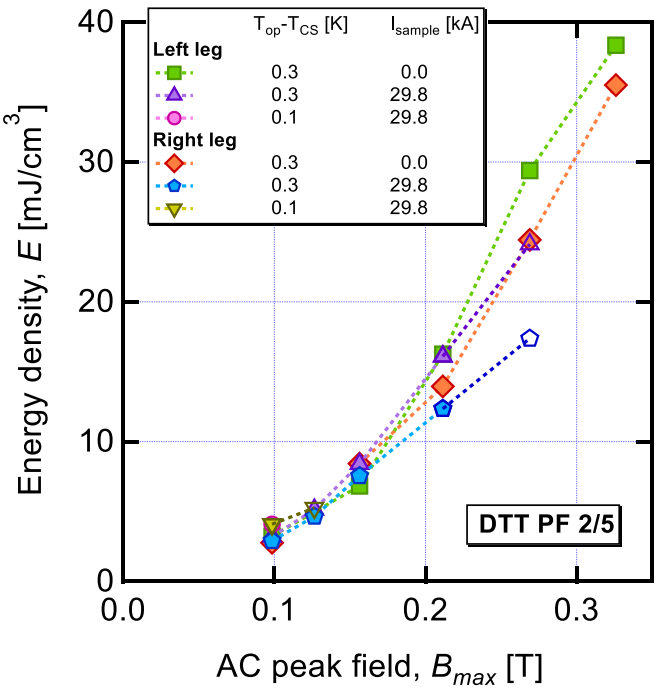


Figure 14. MQE test results of the measurements on Sample PF2/5: the energy deposited on the conductor is plotted as a function of the peak field B_{AC} during the pulse of the AC coil. The empty markers represent for each test the amount of deposited energy that determines a quench in the conductor.

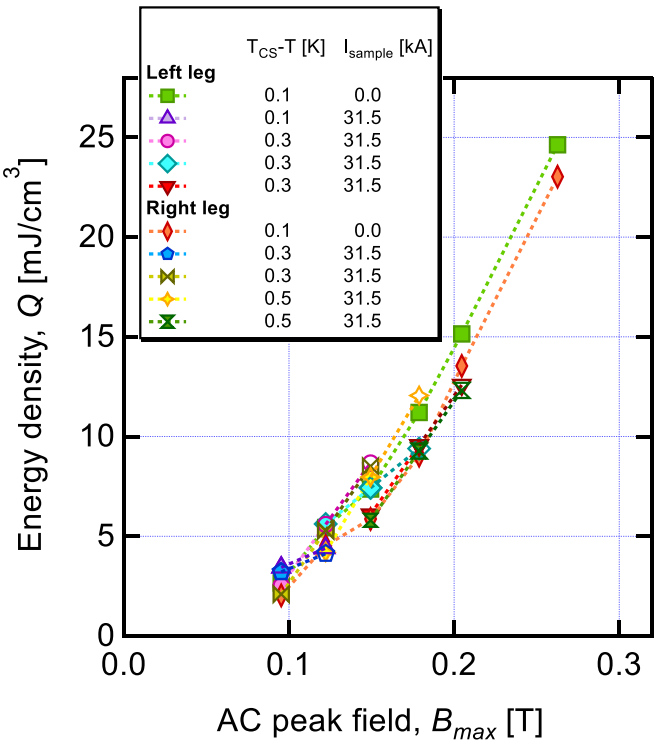


Figure 15. MQE test results of the measurements on Sample PF3/4: the energy deposited on the conductor is plotted as a function of the peak field B_{AC} during the pulse of the AC coil. The empty markers represent for each test the amount of deposited energy that determines a quench in the conductor.

In the MQE tests performed with transport current, the energy is calorimetrically computed for all the external field pulses with increasing B_{AC} except for the one that determines the quench. In this latter case, it is not possible to discriminate between the power generated by the induced eddy currents and the Joule heat generated by the quench.

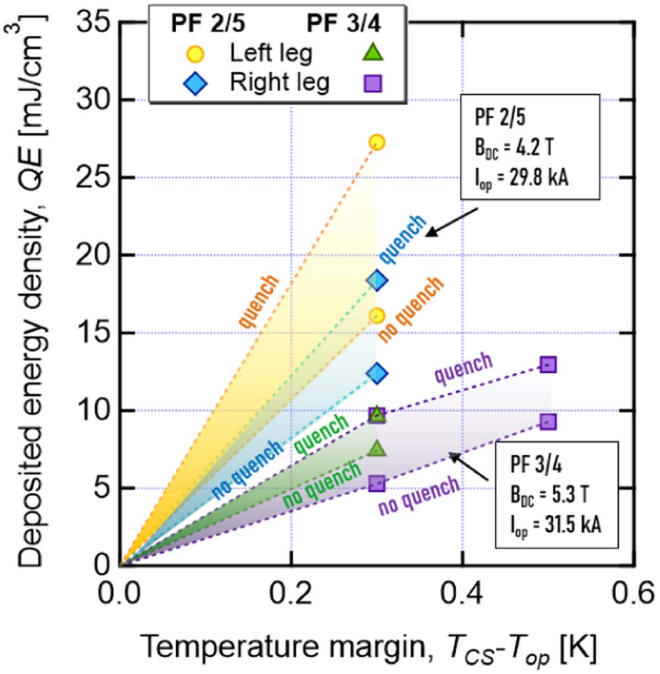


Figure 16. Deposited energy density of samples PF2/5 and PF3/4 as a function of the temperature margin: the dashed line represent the quench/no-quench (recovery) limits. The MQE lies within the dashed lines, inside the colored bands.

Therefore, the value of the quench energy is assessed by a quadratic extrapolation of the data points evaluated calorimetrically [18]. The MQE is then calculated as the average between the maximum energy that allows recovery (last full marker) and the extrapolated deposited energy that determines a quench (empty markers).

For the PF2/5 sample, at a temperature ~0.3 K lower than T_{CS}, the corresponding MQE extracted from the 'calibration' runs is 1.6–2.2 J (i.e. 15–22 mJ cm^{-3} of cable). This value is not far from the MQE of other NbTi conductors, as e.g. the ITER PFEU2 sample [18].

For the PF3/4 sample, at the same ΔT below the T_{CS} (0.3 K), a quench was observed only in the right leg (at 7.5 mJ cm^{-3} of cable, or 0.76 J). To induce quenching in the left leg, we further reduced the temperature of the right leg to T_{CS} – 0.5 K. This allowed us to observe quenching in the left leg at a value of 8.5 mJ cm^{-3} of cable (0.87 J). Finally, we tested the sample at T_{CS} – 0.5 K; this time, as expected, the right leg quenched again (11.1 mJ cm^{-3} of cable, or 1.13 J).

Overall, the MQE of the PF3/4 sample is approximately a factor of 2 lower compared to that of the PF2/5 sample, which reflects the reduced amount of segregated stabilizer in PF3/4.

In figure 16, the deposited energy densities of samples PF2/5 and PF3/4 are plotted as a function of the temperature margin. The dashed lines indicate the boundaries between the quench and recovery (no-quench) regions. The MQE values are located inside the coloured bands.

As shown in table 1, the design temperature margin for PF2/5 is 1.9 K, while for PF3/4 it is 1.7 K. Although extrapolation to these temperature margin values is challenging, figure 16 indicates that the MQE in the PF2/5 sample could exceed 100 mJ cm^{-3}, whereas in PF3/4 it likely does not surpass 50 mJ cm^{-3}. Nevertheless, PF2/5 operates under safer conditions (lower fields and currents), making it inherently more stable. However, to obtain a quantitative assessment of the MQE and temperature margin, dedicated thermohydraulic analyses are required.

8. Conclusions

The experimental campaigns conducted on the NbTi Cable-In-Conduit Conductors of the DTT Poloidal Field coils provided comprehensive insights into their performance at operating conditions. Through a series of cryogenic tests conducted at the SULTAN facility, we evaluated various critical parameters, including DC performance, AC losses, and Minimum Quench Energy (MQE), before and after electromagnetic (EM) cyclic loading.

Key Findings:

1. DC Performance Validation: The DC tests for both samples confirmed their design effectiveness, demonstrating critical currents and current sharing temperatures above the expected operational. The results indicated a slight decrease in DC performance post-cyclic loading, yet remained well within the design acceptance criteria.
2. AC Performance: AC losses on both legs were assessed by gas flow calorimetry and exhibited increasing losses with frequency without reaching a peak or plateau up to 2 Hz, both before and after EM cycling. The $n\tau$ values, determined using the single time constant approximation, were found to be within acceptable values, i.e. ~50 ms in PF2/5 and ~10–150 ms in PF3/4 at a background field of 2 T, without transport current. The values obtained for both samples indicated a slight decrease in $n\tau$ following EM cycling. The presence of transport currents resulted in slightly decreased AC losses for both samples.
3. **Minimum Quench Energy** (**MQE**) **Results**: The MQE tests indicated that Sample PF2/5 achieved values of 1.6–2.2 J (15–22 mJ cm^{-3}), which aligns with the performance expectations for NbTi conductors. Conversely, Sample PF3/4 demonstrated lower MQE values, approximately half that of Sample PF2/5. The temperature margin for both samples, while significant, highlights the need for thorough thermohydraulic analyses to ensure operational safety and stability.

Overall, the results from this study validate the design choices made for the NbTi PF coils of the Divertor Tokamak Test facility, demonstrating robust performance under their challenging operational conditions. Future work will focus on detailed thermohydraulic analyses and further testing to refine the design and enhance the performance of superconducting coils for fusion applications.

Acknowledgments

We thank Marco Breschi for his constructive comments and suggestion on the MQE analysis. This paper, realized with the support of the DTT community, is largely based on the Italian proposal for DTT prepared with contributions of European and international experts [DTT—Divertor Tokamak Test Facility—Interim Design Report R Martone (Ed.) (2019) ISBN: 978-88-8286-378-4].

Data availability statement

The data cannot be made publicly available upon publication because they are owned by a third party and the terms of use prevent public distribution. The data that support the findings of this study are available upon reasonable request from the authors.

ORCID iDs

G De Marzi https://orcid.org/0000-0002-5752-2315
C Fiamozzi Zignani https://orcid.org/0000-0002-3632-2381
H Bajas https://orcid.org/0000-0003-4871-4750
R Bonifetto https://orcid.org/0000-0002-3557-9177
A Di Zenobio https://orcid.org/0000-0002-5086-2333
L Muzzi https://orcid.org/0000-0001-8465-3364
M Ortino https://orcid.org/0000-0001-6509-4763
G M Polli https://orcid.org/0000-0002-9240-2829
G Ramogida https://orcid.org/0000-0001-6485-0213
K Sedlak https://orcid.org/0000-0002-2090-1709
S Turtù https://orcid.org/0000-0002-5493-7785
A Zappatore https://orcid.org/0000-0001-7308-0273

References

[1] Ambrosino R 2021 DTT - divertor tokamak test facility: a testbed for DEMO *Fusion Eng. Des.* **167** 112330
[2] Romanelli F *et al* 2024 Divertor tokamak test facility project: status of design and implementation *Nucl. Fusion* **64** 112015
[3] Federici G *et al* 2018 DEMO design activity in Europe: progress and updates *Fusion Eng. Des.* **136** 729–41
[4] Geng S 2022 An Overview of the ITER Project *J. Phys. Conf. Ser.* **2386** 012012
[5] Lim B, Simon F, Ilyin Y, Gung C Y, Smith J, Hsu Y H, Luongo C, Jong C and Mitchell N 2011 Design of the ITER PF coils *IEEE Trans. Appl. Supercond.* **21** 1918–21

[6] Yoshida K, Tsuchiya K, Kizu K, Murakami H, Kamiya K, Obana T, Takahata K, Peyrot M and Barabaschi P 2010 Development of JT-60SA superconducting magnet system *Physica C: Superconductivity and its Applications* **470** 1727–33
[7] Kumar M, Sedlak K, Sarasola X, Bruzzone P, Della Corte A, Giannini L, Muzzi L and Corato V 2019 Design of DEMO PF coils based on cable-in-conduit conductor *IEEE Trans. Appl. Supercond.* **29** 4200204
[8] Albanese R *et al* 2019 *TT - Divertor Tokamak Test facility - Interim Design Report* ed R Martone, R Albanese, F Crisanti, P Martin and A Pizzuto (Frascati: ENEA) 274
[9] Di Zenobio A *et al* 2017 DTT device: conceptual design of the superconducting magnet system *Fusion Eng. Des.* **122** 299–312
[10] Zoboli L, Anemona A, Zenobio A D, Giannini L, Muzzi L, Romanelli G, Turtu S, Vairo G and Corte A D 2022 Updated structural assessment of the DTT poloidal field coils *IEEE Trans. Appl. Supercond.* **32** 4201505
[11] Fiamozzi Zignani C *et al* 2024 DTT toroidal field conductor samples test in sultan: DC and AC characterization *Supercond. Sci. Technol.* **37** 075009
[12] Bean C P 1964 Magnetization of high-field superconductors *Rev. Mod. Phys.* **36** 31
[13] Bean C P 1962 Magnetization of hard superconductors *Phys. Rev. Lett.* **8** 250–3
[14] Muzzi L *et al* 2010 Pinning properties of commercial Nb-Ti wires described by a 2-components model *IEEE Trans. Appl. Supercond.* **20** 1496–9
[15] Bottura L 2000 Practical fit for the critical surface of NbTi *IEEE Trans. Appl. Supercond.* **10** 1054–7
[16] Bruzzone P, Wesche R, Stepanov B, Cau F, Bagnasco M, Calvi M, Herzog R and Vogel M 2009 Qualification tests and facilities for the ITER superconductors *Nucl. Fusion* **49** 065034
[17] Breschi M, Macioce D and Devred A 2017 Performance analysis of the toroidal field ITER production conductors *Supercond. Sci. Technol.* **30** 1–13055007
[18] Breschi M, Carati D, Bessette D, Devred A, Romano G, Vostner A and Zhou C 2015 Performance analysis of the Nb-Ti conductor qualification samples for the ITER project *Supercond. Sci. Technol.* **28** 115001
[19] Wesche R, Stepanov B and Bruzzone P 2006 Comparison of the DC performance of full- and sub-size NbTi cable-in-conduit conductors *IEEE Trans. Appl. Supercond.* **16** 819–22
[20] AC/DC Module User's Guide COMSOL multiphysics® v5.4. and the structural mechanics module user's guide *COMSOL Multiphysics® v5.4. 2018* (COMSOL AB) 214–61
[21] Wesche R, Stepanov B, Anghel A, Huber S, Pasztor G, Vogel M and Bruzzone P 2004 Self-field effects in NbTi subsize cable-in-conduit conductors *Physica C Supercond* **401** 113–7
[22] Nijhuis A, Ten Kate H H J, Duchateau J L and Bruzzone P 1996 Coupling loss time constants in full-size Nb_3Sn CIC model conductors for fusion magnets *Advances in Cryogenic Engineering Materials* ACRE 42 ed Leonard T Summers (Boston, MA: Springer) pp 1281–8
[23] Muzzi L *et al* 2010 The JT-60SA toroidal field conductor reference sample: Manufacturing and test results *IEEE Trans. Appl. Supercond.* **20** 442–6
[24] Turck B and Zani L 2010 A macroscopic model for coupling current losses in cables made of multistages of superconducting strands and its experimental validation *Cryogenics (Guildf)* **50** 443–9
[25] Nijhuis A, Noordman N H W, Ten Kate H H J, Mitchell N and Bruzzone P 1999 Electromagnetic and mechanical characterisation of ITER CS-MC conductors affected by transverse cyclic loading, 2: interstrand contact resistances *IEEE Trans. Appl. Supercond.* **9** 754–7
[26] Nijhuis A, Ilyin Y, Abbas W, Ten Haken B and Ten Kate H H J 2004 Change of interstrand contact resistance and coupling loss in various prototype ITER NbTi conductors with transverse loading in the twente cryogenic cable press up to 40,000 cycles *Cryogenics (Guildf)* **44** 319–39
[27] Huber M L, Lemmon E W, Bell I H and McLinden M O 2022 The NIST REFPROP database for highly accurate properties of industrially important fluids *Ind. Eng. Chem. Res.* **61** 15449–72